J Mater Sci: Mater Electron **(2023) 34:1739**

The efficient removal towards tetracycline via photocatalytic persulfate activation using the heterostructured UiO-66-NH_2-CA-Cu/g-C_3N_4 composite

Yan Fan[1,2], Lei Wang[1,*], Xueqin Sun[1], Cuili Li[1], and Jiacheng Liu[1,*]

[1] *College of Chemistry and Chemical Engineering, Northwest Normal University, Lanzhou 730070, Gansu, China*
[2] *College of Chemistry and Chemical Engineering, Qinghai Normal University, Xining 810000, Qinghai, China*

Received: 29 April 2023
Accepted: 15 August 2023
Published online: 30 August 2023

ABSTRACT

A series of UiO-66-NH_2-CA-Cu/g-C_3N_4 (UCC_1/CN_x) heterogeneous photocatalysts were constructed via a facile physical mixing treatment of the covalently post-modified MOF (UiO-66-NH_2-CA-Cu) and functional materials g-C_3N_4. The tetracycline removal by the photocatalysis coupled with persulfate activation were studied under white light irradiation. The optimal UCC_1/CN_{20} photocatalyst showed the best photocatalytic performance, in which 94.0% TC could be efficiently eliminated ($k = 0.08669$ min^{-1}) within 30 min. The satisfactory degradation performance could be ascribed to the effective separation of photogenerated electron-hole pairs over the heterogeneous binary structure, which were demonstrated by several characteristic technologies including photoluminescence spectra, electrochemical impedance spectroscopy, transient photocurrent response and Bader charge analysis based on density functional theory calculations. Moreover, a possible mechanism behind the photocatalytic degradation was proposed and further affirmed by the quenching experiments and electron spin resonance measurements. Our work may supply a feasible idea for treating wastewater contained organic pollutants based on the heterogeneous photocatalyst.

1 Introduction

Antibiotics belong to a class of antibacterial drugs applied to cure bacterial infections of humans and animals [1]. Over the past decades, the abuse and accumulation of antibiotics lead to the generation of antibiotic resistant bacteria, which will finally pose a threat to the ecological system and public health [2]. Hence, the emerging contaminants of antibiotics in the aquatic environment have received much attention from environmental researchers [3]. Tetracycline (TC) as a broad-spectrum antibiotic is one of the most widely used antibiotics in some related fields [4]. Thus, it is a tricky problem to develop the efficient and facile treatment technologies for the TC removal from wastewater.

Address correspondence to E-mail: wanglee030@163.com; wanglei030@hotmail.com; jcliu8@nwnu.edu.cn; jcliuchem@163.com

https://doi.org/10.1007/s10854-023-11142-x

Currently, advanced oxidation processes (AOPs) have been perceived as ideal strategies for water treatment, in which the generated reactive radicals can effectively decompose antibiotics into low-toxic and biodegradable products [5, 6]. Compared with the hydroxyl radicals (·OH)-based AOPs, the advanced oxidation processes based on sulphate radicals ($SO_4^{\cdot-}$) show more excellent oxidative degradation ability towards contaminants because the radicals of $SO_4^{\cdot-}$ process higher selectivity and suitability within a wide pH range than those of the ·OH radicals [7, 8]. Generally, peroxydisulfate (PDS, $S_2O_8^{2-}$) or peroxymonosulfate (PMS, HSO_5^-) is employed as a promising oxidant to form free radicals in $SO_4^{\cdot-}$-based AOPs. Although antibiotics can be oxidized into substances with low toxicity by PMS and PDS, the processes usually need intensive energy input [9]. Recently, many studies [10–12] have found that there is a positive synergy between PDS/PMS oxidation and photocatalysis on antibiotics removal. The reasons can be summed up in two aspects: (i) The oxidant of PDS/PMS can be activated by photogenerated electrons to form sulphate radicals and simultaneously (ii) The activity of photocatalysts are improved as PDS/PMS can be served as an electron acceptor facilitating the separation of photogenerated electron-hole pairs.

As a kind of promising photocatalyst, metal-organic frameworks (MOFs) have drawn high attention in the field of heterogeneous photocatalysis over the past decades [13–15]. MOFs have many merits in comparison with traditional inorganic semiconductors. The high porosity of MOFs, for example, is beneficial for the adsorption to pollutants, thus can distinctly promote the subsequent degradation reactions [16]. What's more, MOFs have a remarkable advantage of versatile chemical tunability [17], which provides access to enhance the photocatalytic performance of pristine MOFs by modifying and regulating parent MOFs. As for the modified strategies towards MOFs, implantation of transition metal ions into pristine MOFs through coordinating with ligands has been proved to be one of feasible ways to boost their original photocatalytic activity [18]. For instance, Shi et al. [19] constructed Fe@PCN-224 via a post-synthetic reaction of porphyria MOF PCN-224, and its photo-oxidation ability towards gaseous isopropanol (IPA) was significantly raised relative to pristine PCN-224. The photoactive Zr-based MOF UiO-66-NH_2 exhibits super stability which is able to endure post-synthetic modification (PSM). So according to the need, immobilizing appropriate transition metal ions like Fe^{2+}, Cu^{2+} and Co^{2+} in UiO-66-NH_2 by covalently post-modification seems a fascinating operation. More importantly, the transition metal of Fe^{2+}, Cu^{2+} or Co^{2+} [20] anchored to UiO-66-NH_2 can act as efficient activators for PDS/PMS.

However, single MOFs as photocatalysts usually exhibit the unsatisfied photocatalytic performance due to their inferior conductance [21]. So far, fabricating heterojunction materials by MOFs and other easily conductive semiconductors have been a popular solution to overcome the defect mentioned above [22, 23]. As a metal-free star semiconductor, g-C_3N_4 has received considerable interests by virtue of its intriguing electronic structure, high stability and low cost [24, 25]. Coupling MOFs with g-C_3N_4 often leads to enhanced photocatalytic performance according to the previous researches [26]. In addition to increased conductivity, the construction of heterojunctions by independent MOFs and g-C_3N_4 with the matched positions of valance band (VB) and conduction band (CB) can effectively reduce the recombination of photon-generated carriers [27], which will further promote their photocatalytic activity.

Based on the above background, we firstly designed a strategy for preparing a novel Zr–based MOF, namely UiO-66-NH_2-CA-Cu, through a two-step covalently post-modification of UiO-66-NH_2: (I) UiO-66-NH_2 was functionalized with citric acid (CA) by forming the amide bond, in which the carboxy groups of citric acid can be served as the chelating sites for the immobilization of additional metal ions; (II) further metalized with transition metal ion Cu^{2+} to obtain the chelate complex. The successful incorporation of Cu^{2+} into the parent MOF created new active sites, thus acquiring the enhanced photocatalytic activity. Secondly, for making full use of the advantages of UiO-66-NH_2-CA-Cu and g-C_3N_4, the UiO-66-NH_2-CA-Cu/g-C_3N_4 (UCC_1/CN_x) composites were fabricated via the facile thermal treatment methods. As a result, the efficient photodegradation of tetracycline was easily achieved by as-prepared composites with the addition of PDS under white light irradiation. Besides, the influence of environmental factors (i.e., PDS dosage, photocatalyst dosage, initial pH and co-existing anions) on TC removal over the UCC_1/CN_{20}+PDS system were investigated systematically. Furthermore, the possible mechanism was put forward and then confirmed by the quenching experiments and ESR testing.

2 Experimental

2.1 The details of materials and characterizations

2.1.1 Materials

N,N-dimethylformamide (DMF), acetonitrile (CH_3CN), methanol (CH_3OH) and ethanol (EtOH) were purchased from Tianjin Damao Chemical Reagent Co. Ltd. Copper chloride ($CuCl_2{\cdot}2H_2O$, ≥ 99.0%) and acetic acid were acquired from Shanghai Guangnuo Chemical Reagent Co. Ltd and Tianjin Fengchuan Chemical Reagent Co. Ltd, respectively. Zirconium (IV) chloride ($ZrCl_4$) was obtained from Aladdin Reagent Co. Ltd. Potassium peroxydisulfate ($K_2S_2O_8$, ≥ 99.5%) and sodium hydroxide (NaOH, 96.0%) were purchased from Tianjin Kaitong Chemical Reagent Co. Ltd. Tetracycline hydrochloride (TC) and citric acid monohydrate (CA) were provided by Sinopharm Chemical Reagent Co. Ltd. Hydrochloric acid (HCl, 36.0–38.0%) was purchased from Baiyin Liangyou Chemical Reagent Co. Ltd. 2-Aminoterephthalic acid (NH_2-BDC) and dicyclohexylcarbodiimide (DCC) were obtained from Macklin Biochemical Co. Ltd. All materials used in this paper were commercially available analytical grade without further purification.

2.1.2 Characterizations

The powder X-ray diffraction (PXRD) measurements were recorded using a Bruker D8 ADVANCE powder X-ray diffractometer with Cu-Kα radiation to investigate the crystallographic structure of the samples. Fourier transform infrared (FTIR) spectroscopy was performed on a DIGILAB FTS-3000 spectrometer using KBr pellets. ULTRA Plus scanning electron microscope (SEM) and TECNAI G^2F_{20} STWIN D2278 scanning transmission electron microscope (TEM) were employed to characterize the morphology of the samples. X-ray photoelectron spectroscopy (XPS, Thermo Fisher) was used to analyze the chemical compositions and the chemical oxidation state of elements. The ultraviolet-visible diffuse reflectance spectrum (UV–vis DRS) of the samples were obtained using a UV-2550 ultraviolet-visible spectrophotometer. The photoluminescence (PL) spectra was recorded on a LS-55 fluorescence spectrophotometer. The zeta potentials at different pH were obtained by the laser particle analyzer (ZetasizerNanoZS). The metal contents of Zr and Cu were determined with inductively coupled plasma mass spectroscopy (ICP-MS, Agilent 7900). The electron spin resonance (ESR) spectrum was characterized with a Bruker a300 spectrometer. The light source was provided by 300 W xenon lamp (CEL-HXF300). The concentrations of the TC solutions were monitored by a double-beam ultraviolet spectrophotometer (UV-vis, Persee, TU-1901). CHI-650E electrochemical workstation (Shanghai Chenhua Instrument, China) was employed to examine the photoelectrochemical properties of the samples. For obtaining the photocurrents and electrochemical impedance spectra (EIS), a standard three-electrode detection system was used, in which a Pt wire was served as the counter electrode, Ag/AgCl (saturated KCl) was the reference electrode and an FTO slice was the working electrode. The operating electrolyte employed in the photoelectrochemical study was 0.1 M Na_2SO_4.

2.2 Synthesis of the photocatalyst

2.2.1 Synthesis of UiO-66-NH_2

The preparation method for UiO-66-NH_2 referred to the literature reported previously [28]. Firstly, 2-aminoterephthalic acid (NH_2-BDC)(4.5 mmol, 0.81 g) was completely dissolved in 40 mL N,N-dimethylformamide (DMF) under condition with ultrasonic. Subsequently, $ZrCl_4$ (4.5 mmol, 1.05 g) and 17 mL HAc were added to the above solution. HAc was chosen as the modulator to synthesize UiO-66-NH_2. Then, the mixture was transferred to a 100 mL Telton-lined stainless steel autoclave and maintained the temperature at 120 ℃ for 24 h under autogenous pressure. After natural cooling, the sample was obtained by centrifuging and washing with ultra-pure water three times. The product was placed in the vacuum oven at 60 ℃ overnight for the next use.

2.2.2 Synthesis of UiO-66-NH_2-CA

The post-synthesis modification (PSM) of UiO-66-NH_2 was implemented according to the previous method [29]. Briefly, DCC (4 mmol, 0.83 g) was added to a solution of CA (4 mmol, 0.84 g) in 25 mL CH_3CN, in which DCC as a dehydrating agent could help citric acid convert to citric anhydride

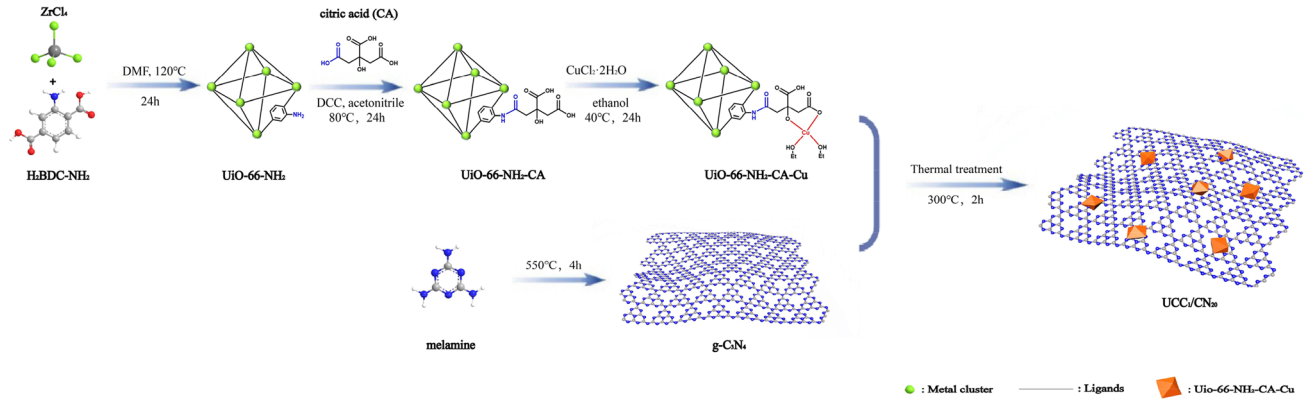

Scheme 1 The synthetic route of the heterostructured UCC_1/CN_{20} nanocomposite

under mild conditions. After that, UiO-66-NH_2 (1 mmol, 1.75 g) was dispersed into the solution and the resultant suspension was kept at 80 ℃ under reflux for 24 h. The introduction of citric acid to the UiO-66-NH_2 framework provided the chelating group for the following installation of catalytic metal ion. The product was centrifuged, rinsed with CH_3CN several times and dried at 60 ℃ overnight.

2.2.3 *Synthesis of UiO-66-NH_2-CA-Cu*

The as-prepared UiO-66-NH_2-CA (0.4 g) was dispersed to a solution of $CuCl_2{\cdot}2H_2O$ (0.17 mmol, 0.029 g) in 20 mL EtOH, then the mixture was heated to 40℃ and kept stirring for 24 h. The catalytic center Cu^{2+} would be immobilized into UiO-66-NH_2-CA by forming a coordinate chelate complex. Further, the final solid was acquired after centrifugation, washing with ethanol three times and thereafter drying under vacuum at 60℃ for 12 h.

2.2.4 *Synthesis of g-C_3N_4*

According to the reported paper [30], g-C_3N_4 was synthesized through the direct pyrolysis of melamine. Typically, 10 g melamine was added into a crucible covered with a lid and then placed in a muffle furnace. The temperature was heated to 550 °C staying for 4 h with a heating rate of 3 °C/min^{-1}. The yellow powder was obtained after cooling down to room temperature.

2.2.5 *Synthesis of UiO-66-NH_2-CA-Cu/g-C_3N_4*

The heterostructured UiO-66-NH_2-CA-Cu/g-C_3N_4 nanocomposite was prepared by the facile methods [31] as follows: As-synthesized UiO-66-NH_2-CA-Cu (10 mg) and g-C_3N_4 with different mass (namely, 100 mg/200 mg/300 mg) were thoroughly ground and dispersed in 50 mL methanol with ultra-sonification for 1 h, and then the solvent was gradually evaporated at 70 °C under magnetic stirring. The obtained sample was further calcined at 300 °C for 2 h (Heating rate: 3 °C/min^{-1}) in a tubular furnace within N_2 atmosphere. The final heterojunction composites with different g-C_3N_4 mass (100 mg/200 mg/300 mg) were labeled as UCC_1/CN_{10}, UCC_1/CN_{20} and UCC_1/CN_{30}, respectively. The composite UCC_1/CN_{20} was used as a representative sample and its synthetic route was illustrated in Scheme 1.

2.3 Photocatalytic experiments

A batch of experiments for tetracycline hydrochloride (TC) degradation under simulated solar light irradiation (300 W xenon lamp without cut-off filter) with the help of potassium peroxydisulfate (PDS) were carried out to evaluate the photocatalytic activity of the target product. Typically, 5 mg of the photocatalyst was added to 50 mL of tetracycline hydrochloride aqueous solution with initial concentration being 20 mg/L (pH = 3.0) in a reactor. After establishing an adsorption-desorption equilibrium in dark for 30 min, 1.0 mM of $K_2S_2O_8$ was added into the reactor under magnetic stirring, and then irradiated

with xenon lamp. The distance between the Xe lamp and the reactor was 10 cm. Next, 3 mL solution was extracted from the reactor every 5 min and then filtered with 0.45 μm filter membranes. The residual concentration of TC was determined by a double-beam ultraviolet spectrophotometer with the maximum absorption wavelength at 356 nm. Moreover, the initial pH values of the solutions were adjusted using 0.1 M HCl or 0.1 M NaOH solutions. As to the cycling tests, the used catalyst was collected by centrifugation, washing with deionized water, and drying for the next round.

3 Results and discussion

3.1 Characterization

3.1.1 XRD patterns of photocatalysts

The crystallographic structures of pure UiO-66-NH_2, UiO-66-NH_2-CA and UiO-66-NH_2-CA-Cu were tested by the X-ray diffraction (XRD). As shown in Fig. 1a, the characteristic peaks of as-prepared UiO-66-NH_2 match well with the simulated XRD pattern [32], indicating the perfect synthesis of UiO-66-NH_2 with high phase purity. After undergoing the post-synthetic modification, the corresponding products UiO-66-NH_2-CA and UiO-66-NH_2-CA-Cu exhibit the similar XRD spectra to the parent MOF UiO-66-NH_2. Their crystallinity is still maintained after the PSM steps, which demonstrates UiO-66-NH_2 possesses an excellent chemical stability. Moreover, the successful introduction of Cu^{2+} to UiO-66-NH_2-CA was verified by ICP-MS analysis. The result shows Zr : Cu ratio of UiO-66-NH_2-CA-Cu is 30.1: 1, and accordingly the copper ion loading is 0.78 wt%.

The XRD patterns of pristine g-C_3N_4, nanocomposites UCC_1/CN_{10}, UCC_1/CN_{20} and UCC_1/CN_{30} are displayed in Fig. 1b. The diffraction peaks at 12.9° (100) and 27.4° (002) for g-C_3N_4 are accord with those reported previously [30]. No obvious characteristic peak belong to UiO-66-NH_2-CA-Cu is found in the XRD pattern of UCC_1/CN_{30}, which may be attributed to the low content of UiO-66-NH_2-CA-Cu. Following the increasement of relative loading of UiO-66-NH_2-CA-Cu, the diffraction peaks caused by UiO-66-NH_2-CA-Cu in composites UCC_1/CN_{20} and UCC_1/CN_{10} become clearly compared with those in UCC_1/CN_{30}. Two-phase composition of UiO-66-NH_2-CA-Cu and g-C_3N_4 in these composites reflect the heterostructured materials are obtained successfully.

3.1.2 FTIR spectra of photocatalysts

The successful introduction of citric acid to UiO-66-NH_2 framework by forming amide bond was also proved by Fourier transform infrared (FTIR) spectroscopy. In Fig. S1a, both the decreasing intensity of the N–H stretching vibration ($v = 3420$ cm^{-1} and $v = 3371$ cm^{-1}) and a newly appeared peak at 1700 cm^{-1} [33] confirm the actual formation of amide (CO–NH) group. The typical absorption regions of g-C_3N_4 is depicted in Fig. S1b. The peaks located at 3000–3400 cm^{-1} and 1200–1700 cm^{-1} are associated with the stretching vibration of N–H and C–N heterocycles [34], respectively. Besides, a peak at 808 cm^{-1} is imputed to the triazine units in g-C_3N_4. As for the FTIR

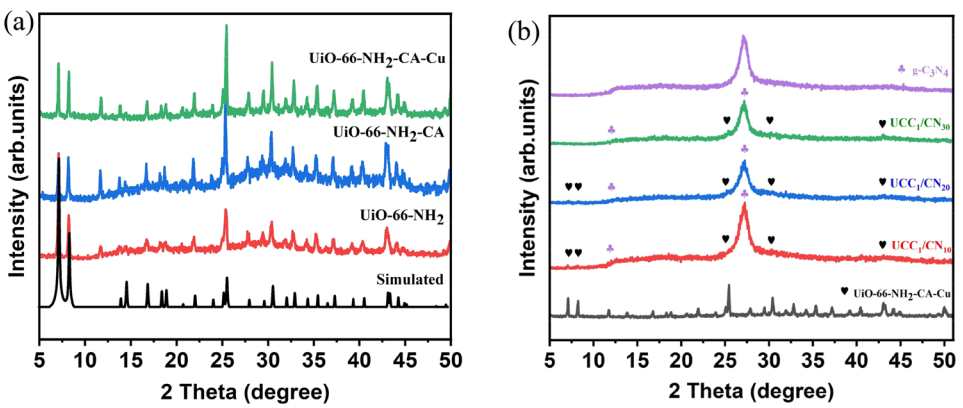

Fig. 1 XRD patterns of **a** UiO-66-NH_2, UiO-66-NH_2-CA and UiO-66-NH_2-CA-Cu and **b** g-C_3N_4, UCC_1/CN_{10}, UCC_1/CN_{20} and UCC_1/CN_{30}

spectroscopy of nanocomposites UCC_1/CN_{10}, UCC_1/CN_{20} and UCC_1/CN_{30} (Fig. S1b), the absorption peak at 808 cm^{-1} display a slight decrease, which suggests there is interaction [34] between UiO-66-NH_2-CA-Cu and g-C_3N_4 in the heterostructured composites.

3.1.3 Morphological analysis of photocatalysts

The morphologies of UiO-66-NH_2 and the two UiO-66-NH_2-based MOFs prepared in this work were examined by SEM measurements. The SEM images of UiO-66-NH_2-CA-Cu (Fig. 2a) and UiO-66-NH_2-CA (Fig. S2b) show that they inherite the octahedron morphology with uniform size from UiO-66-NH_2 (Fig. S2a) after accomplishing the post-synthetic routes. And the pure g-C_3N_4 shows a micron sized layer structure with multiple stacked sheets (Fig. 2b). From the SEM image of UCC_1/CN_{20} in Fig. 2c, UiO-66-NH_2-CA-Cu particle distributes randomly on the surface of g-C_3N_4 and the close combination between them in the composite is observed [35], which indicates the heterojunction is fabricated successfully by employing the simple experimental operation. The TEM image of UCC_1/CN_{20} (Fig. S2c) also could be an evidence for the formation of the heterostructured composite. Additionally, the as-prepared UCC_1/CN_{20} was analysed by the EDS elemental mappings. As shown in Fig. 2d, the uniformly distributed elements C, N, O, Zr and Cu within the binary structure further affirm the acquisition of the nanocomposite.

3.1.4 X-ray photoelectron spectroscopy of photocatalysts

The surface element composition and their chemical state of nanocomposite UCC_1/CN_{20} were explored using XPS technology. As presented in Fig. 3a, there are C, O, N, Zr and Cu coexisting in the as-synthesized sample, which agrees with the result of EDS measurement. The high-resolution spectrum of C 1s (Fig. 3b) is divided into three peaks with binding energies of 288.4 eV, 285.7 eV and 284.7 eV, which are, respectively, attributed to the sp^2 hybridized carbon in the N-containing aromatic ring (N–C=N) [36], the C–N bond of the organic ligand [37] and the sp^2 carbon in the benzoic ring [36]. Figure 3c displays the high-resolution spectra of N 1s. The peaks at 401.6 eV, 400.2 eV and 398.8 eV are mainly due to the groups of –NH, $–NH_2$ [38] and the sp^2 hybridized aromatic nitrogen in C=N–C [36], respectively. In order to examine whether there is a charge transfer after decorating the UiO-66-NH_2-CA-Cu onto the g-C_3N_4, the XPS data of the g-C_3N_4 was also checked. As shown in Fig. S3, the N 1s spectrum of bare g-C_3N_4 exhibits three species, namely N–C=N (397.5 eV), N–$(C)_3$ (398.2 eV) and $–NH_2$ (400.1 eV). The $–NH_2$ binding energy at 400.1 eV shifts to 400.2 eV after mixing the UiO-66-NH_2-CA-Cu with it, which suggests that the lone pair of electrons transfer from $–NH_2$ of g-C_3N_4 to Zr–O group to form NH_2–Zr–O bond. In the high-resolution spectrum of O 1s (Fig. 3d), the first peak located at 532.5 eV [34] is caused by the existence of –COOH group while the second one at 531.5 eV [34] is assigned to the Zr–O bond from UiO-66-NH_2-CA-Cu.

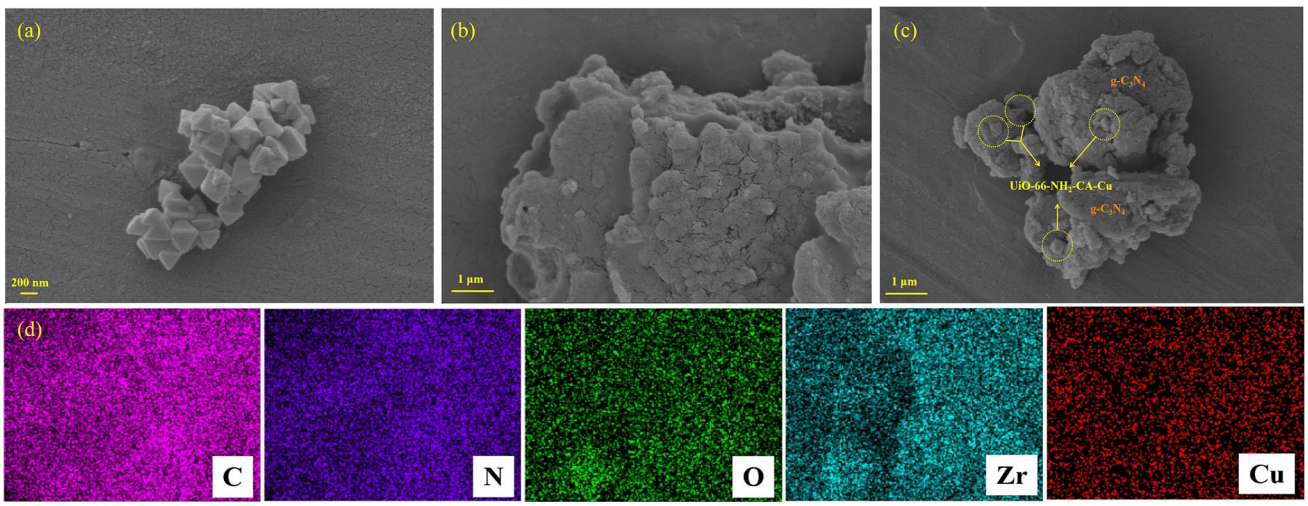

Fig. 2 SEM micrographs of **a** UiO-66-NH_2-CA-Cu, **b** g-C_3N_4, **c** UCC_1/CN_{20} and **d** EDS mapping micrographs of the UCC_1/CN_{20}

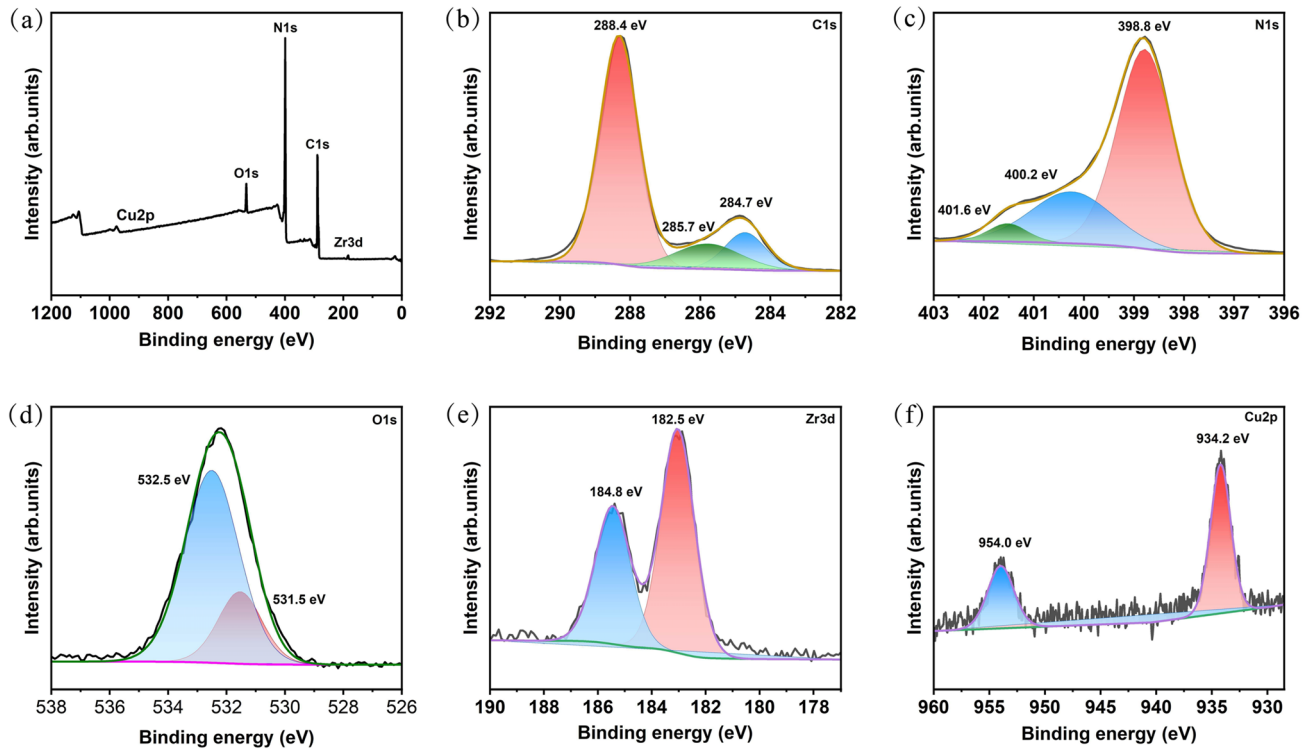

Fig. 3 XPS of the UCC_1/CN_{20}: **a** survey, **b** C 1s, **c** N 1s, **d** O 1s, **e** Zr 3d and **f** Cu 2p spectra

The Zr 3d XPS spectrum (Fig. 3e) presents two obvious peaks appearing at 184.8 and 182.5 eV, which are ascribed to Zr $3d_{3/2}$ and Zr $3d_{5/2}$ [39], respectively. The result reveals Zr^{4+} oxidation state occur in the heterostructured composite. From the Cu 2p high-resolution spectra in Fig. 3f, the binding energies of 954.0 eV (Cu $2p_{1/2}$) and 934.2 eV (Cu $2p_{3/2}$) are the typical values for Cu^{2+} in Cu(II)-CA [40].

3.2 Photocatalytic performances

3.2.1 Photocatalytic TC degradation

To evaluate the photocatalytic performances of the as-synthesized samples, a batch of control experiments with various reactive conditions, including UiO-66-NH_2+PDS, UiO-66-NH_2-CA+PDS, UiO-66-NH_2-CA-Cu+PDS, g-C_3N_4+PDS, UCC_1/CN_{10}+PDS, UCC_1/CN_{20}+PDS, UCC_1/CN_{30}+PDS, UCC_1/CN_{20}, PDS and UCC_1/CN_{20}+PDS (dark), were employed. TC being one of the most usual antibiotics was chosen as the target contaminant, and the changes of its concentration following photocatalytically degradation were detected by UV–Vis spectroscopy. As shown in Fig. 4a, PDS can be activated in varying degrees with white light irradiation when different photocatalyst exists. Concretely, the system of UiO-66-NH_2-CA-Cu+PDS exhibits a higher TC removal efficiency (70.5%) when compared with those of UiO-66-NH_2+PDS (59.5%) and UiO-66-NH_2-CA+PDS (42.0%) system. Correspondingly, the reaction kinetics (Fig. 4b, c) obtained from pseudo-first-order model ($-\ln[C/C_0] = kt$) show the order of UiO-66-NH_2-CA-Cu + PDS ($k = 0.03783\ min^{-1}$) > UiO-66-NH_2+PDS ($k = 0.02824\ min^{-1}$) > UiO-66-NH_2-CA+PDS ($k = 0.01693\ min^{-1}$). The above results distinctly indicate that the photodegradation ability of the as-prepared UiO-66-NH_2-CA-Cu is improved after suffering the two-step post-modification. In UiO-66-NH_2-CA-Cu, the introduction of the chelating agent CA can effectively prevent the precipitation of Cu^{2+} in the process of photocatalytic degradation [41], and simultaneously the coordinated copper ion can immensely boost the migration of charge carriers [42]. Thus, this microenvironment tailoring towards UiO-66-NH_2 is a rational way to enhance its original photocatalytic ability.

The TC degradation efficiency by the system of g-C_3N_4+PDS reaches up to 65.5% with $k = 0.03573\ min^{-1}$ within 30 min. Specifically, the best photocatalytic

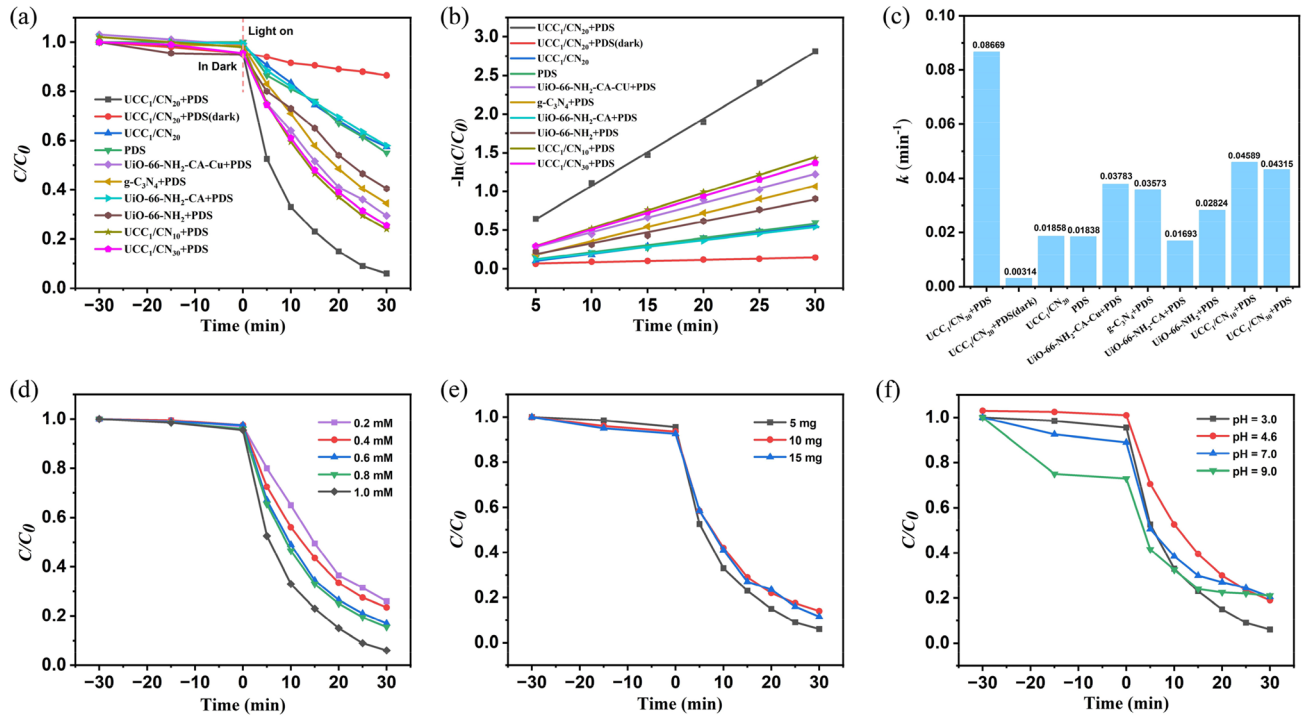

Fig. 4 **a** Photodegradation of tetracycline hydrochloride (TC) under simulated solar light. Condition: (photocatalyst) = 0.1 g/L, (PDS) = 1.0 mM, pH = 3.0 and. (TC) = 0.02 g/L; **b** Pseudo-first-order kinetics curves over different conditions; **c** The corresponding *k* values over different conditions; **d** Effect of PDS concentration on the TC degradation. Condition: (photocatalyst) = 0.1 g/L, pH = 3.0 and (TC) = 0.02 g/L; **e** Effect of photocatalyst concentration on the TC. degradation. Condition: (PDS) = 1.0 mM, pH = 3.0 and (TC) = 0.02 g/L and **f** Effect of initial pH on the TC degradation. Condition: (photocatalyst) = 0.1 g/L, (PDS) = 1.0 mM and (TC) = 0.02 g/L

activity towards TC (removal efficiency: 94.0%, $k = 0.08669\ min^{-1}$) is acquired when the photocatalyst composite UCC_1/CN_{20} is used as a PDS activator in the UCC_1/CN_{20}+PDS system. The excellent performance of UCC_1/CN_{20} can be ascribed to the effectively inhibition for the recombination of electron-hole pairs within the heterogeneous binary structure, which will be demonstrated in the text below. Although the degradation performance of composites UCC_1/CN_{10} (removal efficiency: 76.0%, $k = 0.04589\ min^{-1}$) and UCC_1/CN_{30} (removal efficiency: 74.5%, $k = 0.04315\ min^{-1}$) is inferior to that of UCC_1/CN_{20}, their photocatalytic ability still better than pure UiO-66-NH_2-CA-Cu or g-C_3N_4. When the single UCC_1/CN_{20} or PDS is employed in the photodegradation system, the removal efficiency respectively declines to 42.5% ($k = 0.01858\ min^{-1}$) and 45.0% ($k = 0.01838\ min^{-1}$), which further indicates that the combination of photocatalyst UCC_1/CN_{20} and PDS in the coexistence system plays the synergistic effect on efficiently removing TC from water. In the system of UCC_1/CN_{20}+PDS (dark), both the degradation efficiency (13.5%) and its reaction rate ($0.00314\ min^{-1}$) are far less than those in the UCC_1/CN_{20}+PDS system, implying that light-induced carriers and/or radicals significantly contribute to the degradation of tetracycline. Furthermore, compared with the TC degradation system involved in the recent reports [43–46] (Table S1), UCC_1/CN_{20}+PDS system shows relative ascendancy over them.

3.2.2 *Influence of PDS concentration on TC degradation*

PDS dosage is a key parameter in TC degradation process as it can directly affect the generation of free radicals. Thus, the degradation performance of the UCC_1/CN_{20}+PDS system with different PDS concentration was studied. As illustrated in Fig. 4d and Fig. S4a, only 74.0% of the degradation efficiency ($k = 0.04627\ min^{-1}$) is received when 0.2 mM PDS is added to the system, and along with the PDS concentration increases to 1.0 mM, the degradation efficiency accordingly reaches

up to 94.0% and simultaneously its reaction rate is enhanced to 0.08669 min^{-1} (about 1.87 times higher than that of the UCC_1/CN_{20}+PDS system with 0.2 mM PDS). In general, the more PDS is involved in the degradation system, the more amount of reactive oxygen species (such as $SO_4^{\cdot-}$ and ·OH) will be produced, which are closely connected with the advanced oxidation process [47]. Consequently, the best degradation performance is gained when 1.0 mM of the PDS concentration is used in the system. Also, 1.0 mM is treated as the optimal PDS concentration for the next experiments.

3.2.3 *Influence of photocatalyst concentration on TC degradation*

Figure 4e and Fig. S4b displayed the change of the TC degradation efficiency and corresponding *k* values accompanied by the increase of UCC_1/CN_{20} concentration under a certain amount of PMS (1.0 mM). TC removal rates show a slight decrease when the photocatalyst dosage increases from 5 to 15 mg. Specifically, the removal efficiency is 94.0%, 86.0% and 88.5% with the dosage of UCC_1/CN_{20} at 5 mg, 10 mg and 15 mg, respectively. The reason is that excessive catalyst will not only enlarge the scattering activity of the system towards light [48] but also lead to the tardiness in mass transfer [49]. Thus, 5 mg is considered as the optimal concentration of photocatalyst used in the degradation experiments.

3.2.4 *Influence of initial pH on TC degradation*

The pH value of the system is a vital contributing factor for the TC removal as it can make a impact on the generation of free radicals. Four initial pH values respectively at 3.0, 4.6 (the unadjusted one), 7.0 and 9.0 were chosen to explore the influence on photocatalysis degradation over UCC_1/CN_{20}+PDS system. As shown in Fig. 4f and Fig. S4c, the best degradation effect (removal efficiency: 94.0%, $k = 0.08669\ min^{-1}$) is obtained with the environmental pH being 3.0, and the removal rate of TC gradually decreases as the solution pH increase from 3.0 to 9.0. More specifically, the TC removal rate drops to 79.0% within 30 min at pH = 9.0. The reason for this phenomenon is mainly to blame [50] that the system with an acidic condition is favorable for the formation of $SO_4^{\cdot-}$ free radical, which refers to Eqs. (1) and (2). Thus, all the degradation experiments are conducted with the pH pre-adjusting to 3.0. Throughout the removal rates got under different pH values, the least desirable result (pH = 9.0) still maintains higher than 79%, which reveals that the decomposition of TC over UCC_1/CN_{20} + PDS system can work universally with a wide pH range.

$$S_2O_8^{2-} + H^+ \rightarrow HS_2O_8^- \quad (1)$$

$$HS_2O_8^- + e^- \rightarrow SO_4^{\cdot-} + SO_4^{2-} + H^+ \quad (2)$$

3.2.5 *Influence of co-existing anions on TC degradation*

Several typical anions (NO_3^-, Cl^- and $H_2PO_4^-$) were added to the photoreactor to examine the practical application about the UCC_1/CN_{20}+PDS system. Fig. S5a, b illustrate that the introduction of all inorganic anions has a negative effect on TC degradation. The removal rates and *k* values obey the order of no anions (94.0%, 0.08669 min^{-1}) > Cl^- (83.0%, 0.05504 min^{-1}) > NO_3^- (82.0%, 0.05186 min^{-1}) > $H_2PO_4^-$ (80.0%, 0.04878 min^{-1}). The inorganic anions may act as radical scavengers to consume reactive oxygen species, or transform the free radicals to less active ones [51], thus weakening the degradation ability of the UCC_1/CN_{20}+PDS system. However, the fall of degradation performance is always kept in an acceptable range after adding the inorganic anions, suggesting the UCC_1/CN_{20}+PDS system possesses a significant ability against interference.

3.2.6 *Reusability and stability of MIL-125(Ti)-NH_2-Sal-Fe*

Besides the photocatalytic activity, the stability of catalyst is equally important for the practical application. As displayed in Fig. 5a, the removal efficiency drops from 94.0% (the first run) to 83.0% (the fourth run), the reason for the decrease may lie in the active sites of the catalyst are covered by the intermediates from TC decomposition during the degradation process [52]. Furthermore, the XRD pattern, FTIR spectra and SEM image of the used UCC_1/CN_{20} were examined. The results presented in Fig. 5b, d show an insignificant change compared with those of the fresh UCC_1/CN_{20}, implying the catalyst UCC_1/CN_{20} still keeps its stability after the repeated reactions.

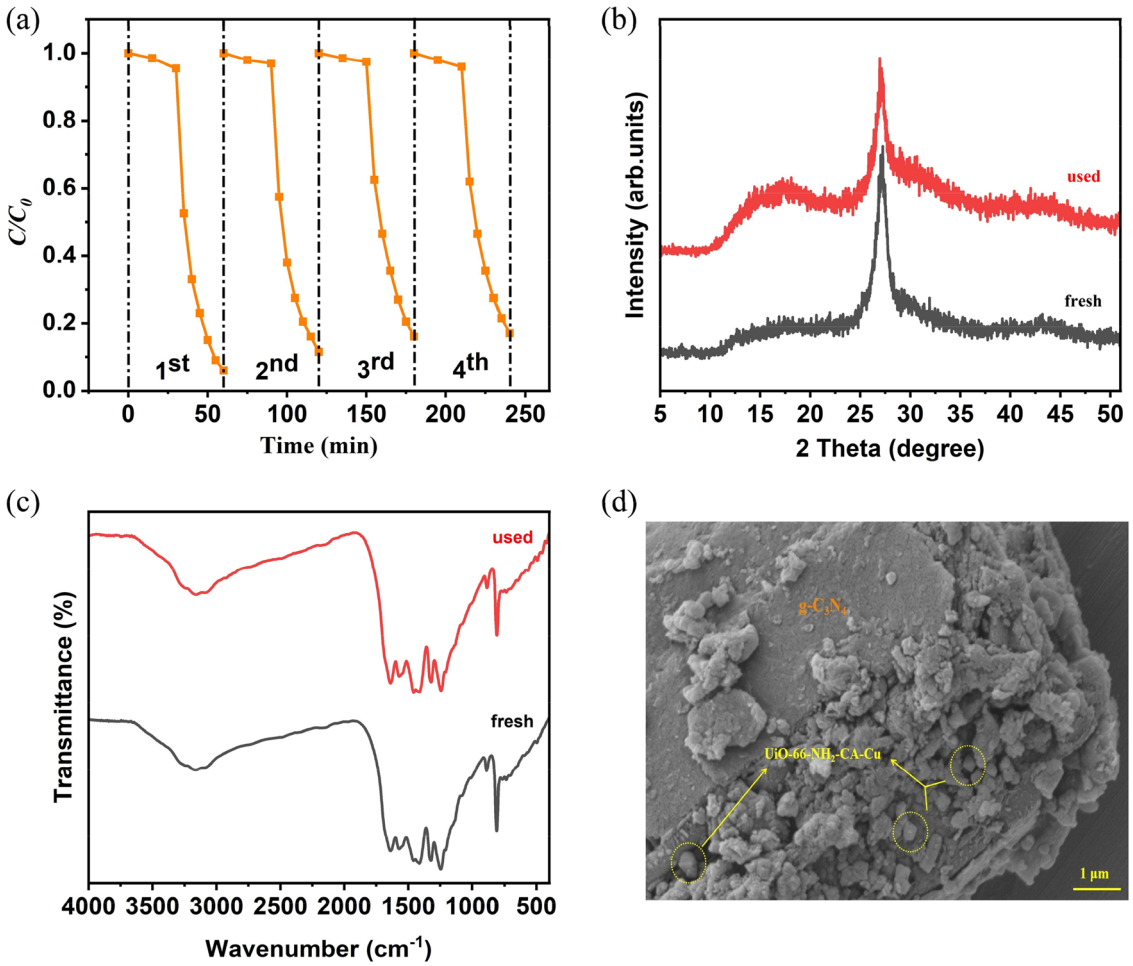

Fig. 5 **a** Reusability experiments over UCC_1/CN_{20}+PDS system for TC degradation. Condition: (photocatalyst) = 0.1 g/L, (PDS) = 1.0 mM, pH = 3.0 and (TC) = 0.02 g/L; **b** PXRD patterns; **c** FTIR spectras of the UCC_1/CN_{20} after the cyclic experiments and **d** SEM micrograph of the UCC_1/CN_{20} after the cyclic experiments

3.3 The possible mechanism for photocatalytic reaction

The optical and photoelectrochemical properties of the photocatalysts were investigated to get a deep understanding of the generation and transfer of the photo-induced carriers within photocatalysts. As seen in Fig. 6a, the as-synthesized UiO-66-NH_2-CA-Cu displays a strong absorption with the range of 200–450 nm, and the absorption edge of the pristine g-C_3N_4 is at around 500 nm. As for the composites UCC_1/CN_{10}, UCC_1/CN_{20} and UCC_1/CN_{30}, their absorption edges show the slight red shift compared with that of UiO-66-NH_2-CA-Cu, indicating the light absorption of the composites are marginally enhanced [53, 54]. Additionally, the E_g values of UiO-66-NH_2-CA-Cu and g-C_3N_4 are respectively at 2.84 eV and 2.74 eV according to the approach of Tauc plot (Fig. 6b). The flat-band potential (E_{FB}) is confirmed by the Mott–Schottky plots (Fig. 6c, d), specifically, the E_{FB} locates at − 0.82 V for UiO-66-NH_2-CA-Cu and − 1.16 V for g-C_3N_4. Therefore, their flat-band potential vs. NHE is respectively − 0.21 V and − 0.55 V according to the conversion formula [55, 56] [E_{FB} (vs. NHE) = E_{FB} (vs. Ag/AgCl) + $E_{Ag/AgCl}$ (vs. NHE) + 0.0591 × pH]. In general, E_{FB} is higher than the conduction band potential (E_{CB}) by 0.2 V with regard to *n*-type semiconductor [55, 56], hence the E_{CB} of UiO-66-NH_2-CA-Cu and g-C_3N_4 is − 0.41 V and − 0.75 V, respectively. Combining with the E_g values acquired by UV–Vis DRS spectra, the corresponding valence band potential (E_{VB}) for UiO-66-NH_2-CA-Cu and g-C_3N_4 can be calculated as 2.43 V

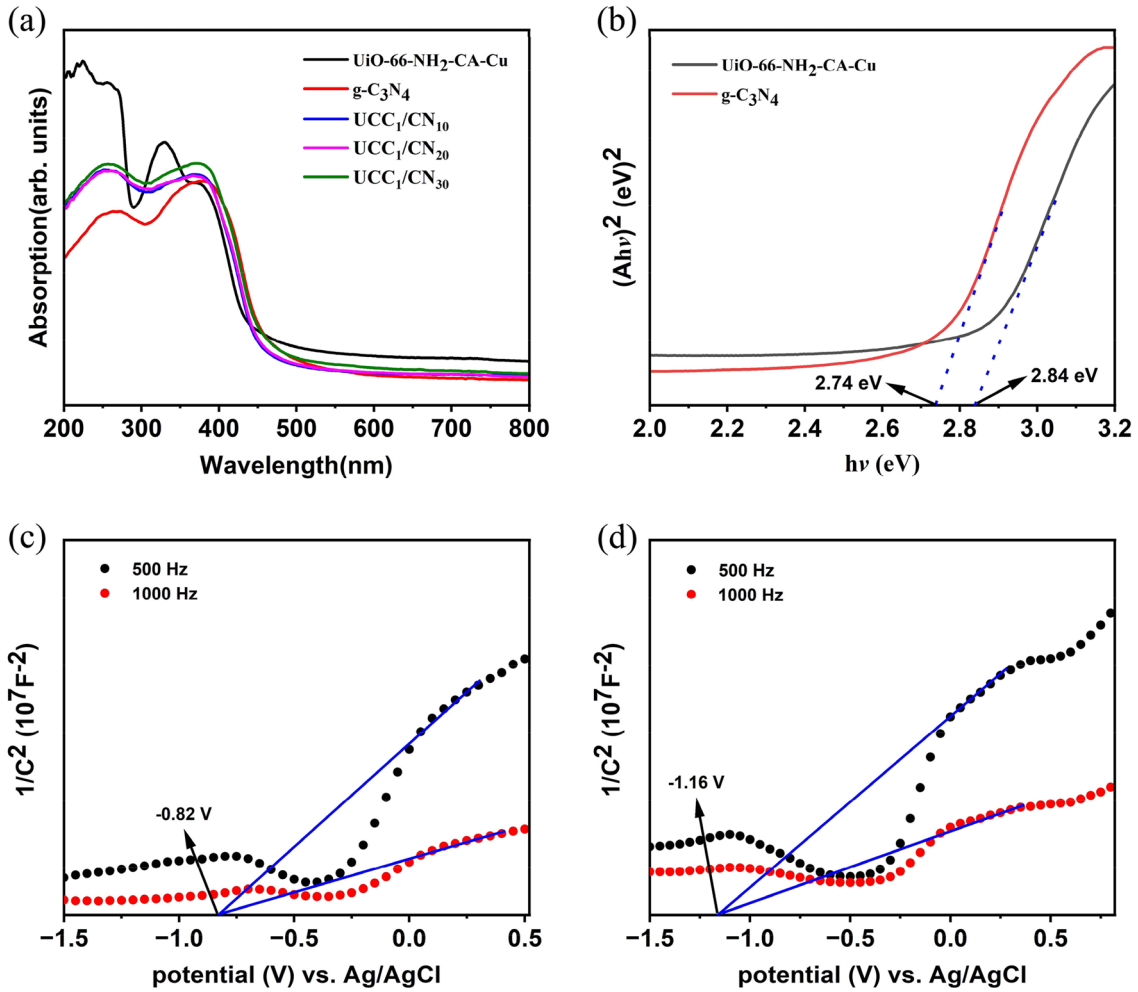

Fig. 6 **a** UV–Vis DRS spectras of the photocatalysts; **b** Band gap energy of UiO-66-NH_2-CA-Cu and g-C_3N_4; Mott–Schottky plots of **c** UiO-66-NH_2-CA-Cu and **d** g-C_3N_4

and 1.99 V with the formula of $E_{VB} = E_{CB} + E_g$. Furthermore, Bader charge analysis based on DFT calculations was employed to investigate the interfacial charge redistribution after the formation of the heterojunction. As shown in Fig. S6, the electrons are transferred from g-C_3N_4 to UiO-66-NH_2 within the composite and the electron transfer value is calculated as 0.5, thus, the as-obtained UCC_1/CN_{20} composite can form a type-II heterojunction.

The photongenerated carrier separation efficiency of the photocatalysts were evaluated by photoluminescence (PL) spectra, electrochemical impedance spectroscopy (EIS) and transient photocurrent response. In Fig. 7a, PL analysis indicates that the photoluminescence intensities of any composites are reduced obviously compared with that of the single component (UiO-66-NH_2-CA-Cu and g-C_3N_4), and the composite UCC_1/CN_{20} shows the lowest fluorescence intensity among them, which demonstrates electron-hole pair recombination is effectively suppressed within the heterojunction thus resulting to the longest lifetime of the photogenerated carrier [57]. From the result of EIS (Fig. 7b), the Nyquist radius of the as-prepared materials follow the order: UiO-66-NH_2-CA-Cu > g-C_3N_4 > UCC_1/CN_{30} > UCC_1/CN_{10} > UCC_1/CN_{20}, directly suggesting the lowest resistance over UCC_1/CN_{20} during the process of charge transfer [58]. Figure 7c presents that the UCC_1/CN_{20} composite owns the highest photocurrent value of any photocatalyst obtained in this work, indicating that the fabrication of UCC_1/CN_{20} is conducive to boosting the migration rate of photo-generated carriers [59]. All of the above-mentioned results are well in accordance with the degradation performances of the photocatalysts.

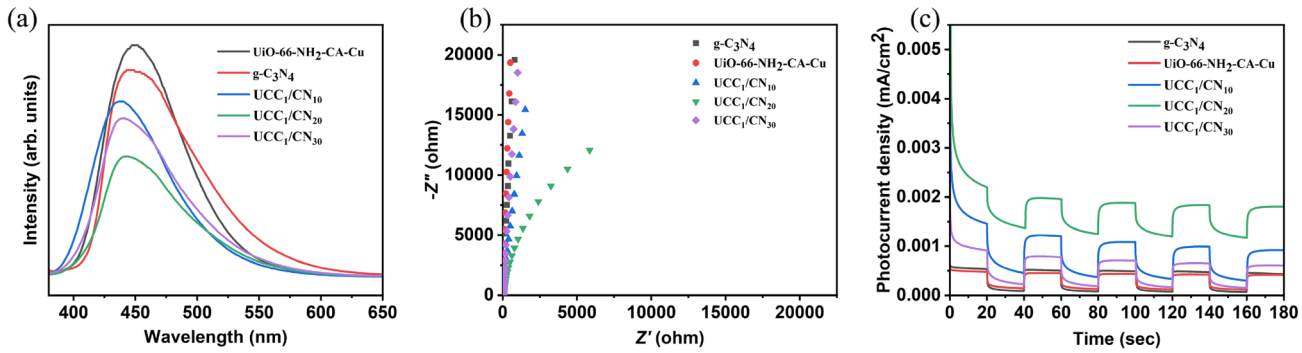

Fig. 7 **a** Photoluminescence spectras; **b** Nyquist impedance plots and **c** Transient photocurrent responses of the photocatalysts

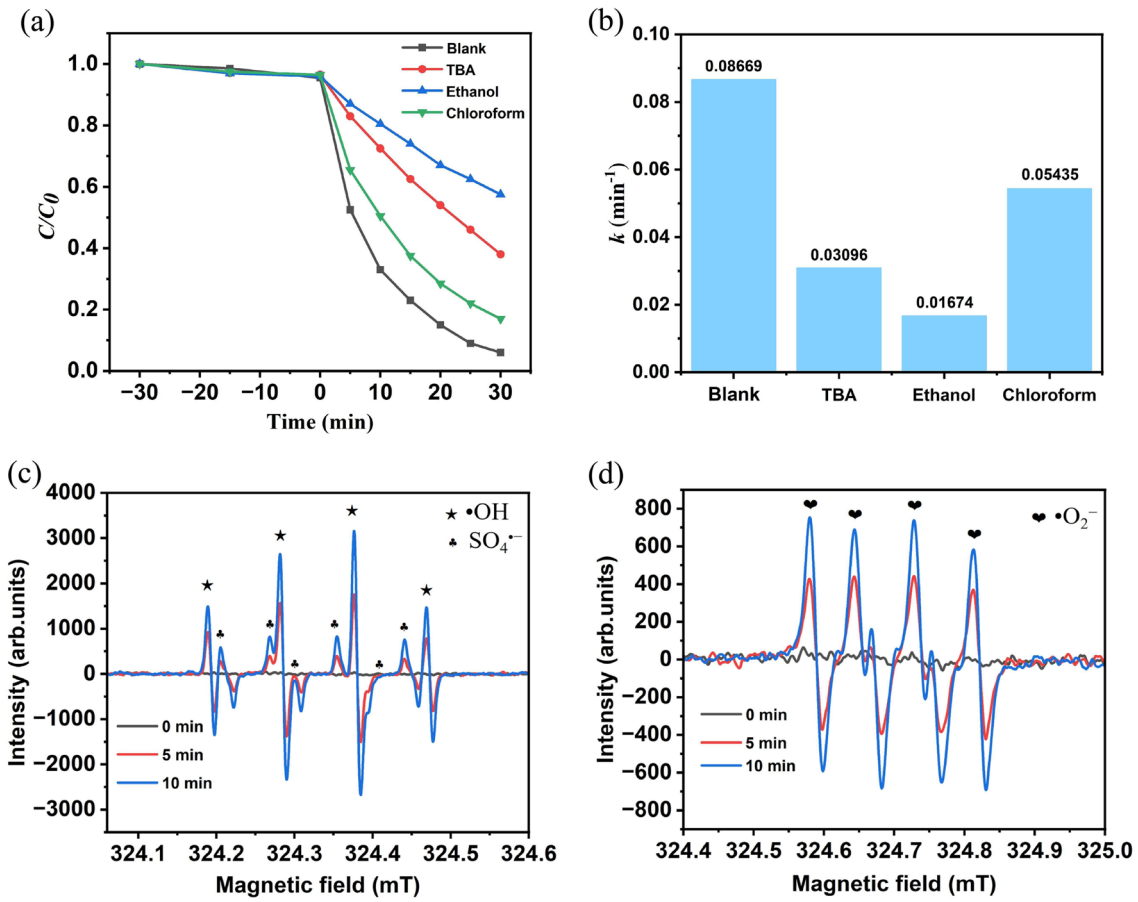

Fig. 8 **a** The quenching experiments for TC degradation over the UCC_1/CN_{20}+PDS system; **b** The corresponding *k* values in the quenching experiments; electron spin resonance (ESR) spectras of **c** DMPO-·OH, DMPO-$SO_4^{\cdot-}$ and **d** DMPO-$\cdot O_2^-$ in the UCC_1/CN_{20}+PDS system

Quenching experiments were carried out to check the main active species over the UCC_1/CN_{20}+PDS system for TC degradation. In general, t-butanol (TBA) [60] and chloroform [61] are respectively served as the scavenger for ·OH and $\cdot O_2^-$, while EtOH can simultaneously quench ·OH and $SO_4^{\cdot-}$ due to its high rate constants towards ·OH ($k_{\cdot OH} = 1.9 \times 10^9\ M^{-1}\ s^{-1}$) and $SO_4^{\cdot-}$ ($k_{SO4\cdot-} = 1.6 \times 10^7\ M^{-1}\ s^{-1}$) [62, 63]. As shown in Fig. 8a, b, quenching tests reveal that the TC removal efficiency respectively drops from 94.0%

($k = 0.08669\ min^{-1}$) to 62.0% ($k = 0.03096\ min^{-1}$), 42.5% ($k = 0.01674\ min^{-1}$) and 83.0% ($k = 0.05435\ min^{-1}$) after adding the scavenger TBA, EtOH and chloroform, which illustrates that the three active species ·OH, $SO_4^{\cdot-}$ and $\cdot O_2^-$ are involved in the TC decomposition with the contribution order of ·OH > $SO_4^{\cdot-}$ > $\cdot O_2^-$. For verifying the results of quenching experiments, electron spin resonance (ESR) measurements were further applied to detect the signals of free radicals during the degradation process. Figure 8c, d show that the signals for ·OH, $SO_4^{\cdot-}$ and $\cdot O_2^-$ are barely captured in the dark condition, while the intensity of characteristic peaks for DMPO-·OH, DMPO-$SO_4^{\cdot-}$ and DMPO-$\cdot O_2^-$ becomes stronger as the irradiation time prolongs in the ESR tests. The results also prove that the composite UCC_1/CN_{20} has an excellent photocatalytic activation ability within the UCC_1/CN_{20}+PDS system.

Based on the above experimental results, the photocatalytic mechanism over the UCC_1/CN_{20}+PDS system was tentatively inferred and presented in Fig. 9. The photogenerated electrons and holes are formed within the composite UCC_1/CN_{20} under white light illumination according to the Eq. (3). Subsequently, the photoexcited electrons located in the CB of g-C_3N_4 (− 0.75 V vs. NHE) move to the lowest unoccupied molecular orbital (LUMO) of UiO-66-NH_2-CA-Cu (-0.41 V vs. NHE) by the means of interface electron behavior. Considering the LUMO of UiO-66-NH_2-CA-Cu is more negative than the redox potential of $O_2/\cdot O_2^-$ (− 0.33 V vs. NHE) [64], thus the dissolved oxygen can be converted to the free radical of $\cdot O_2^-$ after obtaining the excited electrons (Eq. 4). At the same time, the excited electrons are captured by PDS, which directly causes the formation of $SO_4^{\cdot-}$ free radical by Eq. (5). The PDS activation not only conduces to the decomposition of TC but also restrains the recombination of electron-hole pairs within the photocatalyst [65]. Besides, the photo-excited electrons can transfer to the Cu^{2+} centers in the UCC_1/CN_{20} (Eq. 6) through the way of ligand to metal charge transfer (LMCT) [51, 66]. The obtained Cu^+ ions can further activate PDS following Eq. (7), then the reaction product Cu^{2+} ions are used to support the photocatalytic cycles and the another product, namely $SO_4^{\cdot-}$ free radicals, are employed to generate the active species of ·OH (Eq. 8) [67]. Ultimately, the active oxygen species of ·OH, $SO_4^{\cdot-}$ and $\cdot O_2^-$ together participate in the degradation process, and the efficient TC removal owes to the synergistic effects between photocatalysis and persulfate activation occurred in the UCC_1/CN_{20} + PDS system.

$$UCC_1/CN_{20} + h\nu \rightarrow h^+ + e^- \quad (3)$$

$$O_2 + e^- \rightarrow \cdot O_2^- \quad (4)$$

$$S_2O_8^{2-} + e^- \rightarrow SO_4^{\cdot-} + SO_4^{2-} \quad (5)$$

$$Cu^{2+} + e^- \rightarrow Cu^+ \quad (6)$$

$$Cu^+ + S_2O_8^{2-} \rightarrow Cu^{2+} + SO_4^{\cdot-} + SO_4^{2-} \quad (7)$$

$$SO_4^{\cdot-} + H_2O \rightarrow \cdot OH + SO_4^{2-} + H^+ \quad (8)$$

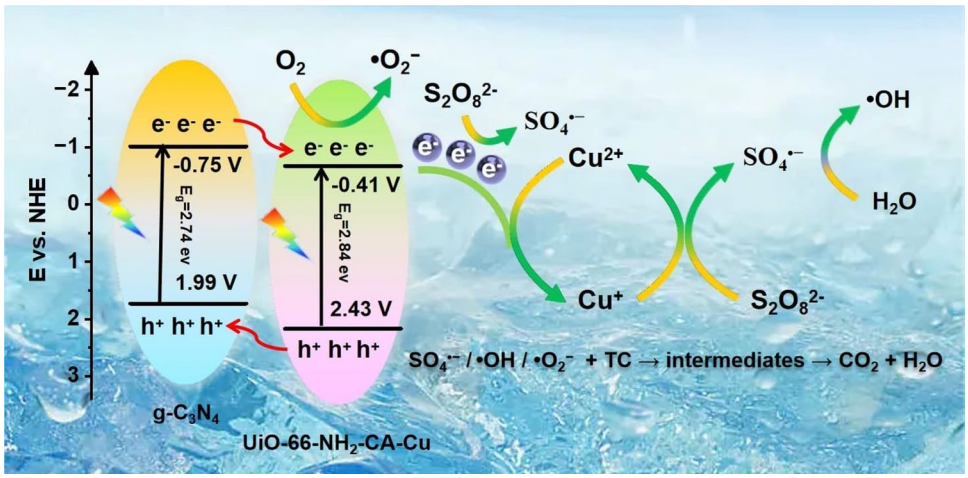

Fig. 9 Possible mechanism for TC degradation by the UCC_1/CN_{20}+PDS system

4 Conclusions

In summary, the heterogeneous photocatalyst UCC$_1$/CN$_{20}$ was successfully fabricated to activate PDS for the efficient removal towards TC under white light irradiation. The formation of nanocomposite facilitates the migration and separation of photogenerated carriers, thus boosting the degradation performance over the UCC$_1$/CN$_{20}$+PDS system. The key factors that influenced the degradation efficiency including PDS dosage, photocatalyst dosage, initial pH and co-existing anions was explored systematically. Moreover, the UCC$_1$/CN$_{20}$ composite maintained its stability well after the cycle experiments, demonstrating that the photocatalyst had the possibility of practical application. The findings in this work provide a novel insight into rational design for MOFs/g-C_3N_4 hybrid photocatalysts, which broadens the application of the combination between photocatalysis and PDS activation for the water environment remediation.

Acknowledgements

This work was financially supported by the National Natural Science Foundation of China (22162023 and 21761031), National Natural Science Foundation of Gansu province (No.20JR5RA523), Industrial Support Plan Project of Colleges in Gansu Province (2021CYZC-17), the Key Science and Technology Foundation of Gansu Province (20YF3GA021), the Innovation Funding Program of Universities of Gansu province (2020B-091), the Promotion Project of Young-Teacher Research capacity of Northwest Normal University (NWNU-LKQN-18-5) and the Natural Science Young Scholars Research Fund Project of Qinghai Normal University (2020QZR019).

Author contribution

YF: methodology, investigation, writing—original draft. LW: supervision, writing—original draft, investigation. XS: methodology, investigation. CL: investigation. JL: supervision, conceptualization, project administration, writing—review and editing.

Funding

This study was funded by the National Natural Science Foundation of China (22162023 and 21761031), National Natural Science Foundation of Gansu province (No. 20JR5RA523), Industrial Support Plan Project of Colleges in Gansu Province (2021CYZC-17), the Key Science and Technology Foundation of Gansu Province (20YF3GA021), the Innovation Funding Program of Universities of Gansu province (2020B-091), and the Promotion Project of Young-Teacher Research capacity of Northwest Normal University (NWNU-LKQN-18-5).

Data availability

The authors confirm that the data supporting the findings of this study are available within the article (and/or its supplementary materials).

Declarations

Competing interests The authors declare that they have no known competing financial interests or personal relationships that would influence the work reported in this paper.

Supplementary Information The online version contains supplementary material available at https://doi.org/10.1007/s10854-023-11142-x.

References

1. K. Kummerer, Antibiotics in the aquatic environment–a review–part I. Chemosphere **75**, 417–434 (2009)
2. V.K. Sharma, N. Johnson, L. Cizmas, T.J. McDonald, H. Kim, A review of the influence of treatment strategies on antibiotic resistant bacteria and antibiotic resistance genes. Chemosphere. **150**, 702–714 (2016)
3. N.H. Tran, M. Reinhard, K.Y. Gin, Occurrence and fate of emerging contaminants in municipal wastewater treatment plants from different geographical regions—a review. Water Res. **133**, 182–207 (2018)
4. H. Shi, J. Ni, T. Zheng, X. Wang, C. Wu, Q. Wang, Remediation of wastewater contaminated by antibiotics. A review. Environ. Chem. Lett. **18**, 345–360 (2019)

5. F.C. Moreira, R.A.R. Boaventura, E. Brillas, V.J.P. Vilar, Electrochemical advanced oxidation processes: a review on their application to synthetic and real wastewaters. Appl. Catal. B **202**, 217–261 (2017)
6. I. Velo-Gala, J.A. Pirán-Montaño, J. Rivera-Utrilla, M. Sánchez-Polo, A.J. Mota, Advanced oxidation processes based on the use of UVC and simulated solar radiation to remove the antibiotic tinidazole from water. Chem. Eng. J. **323**, 605–617 (2017)
7. V. Hasija, V.H. Nguyen, A. Kumar, P. Raizada, V. Krishnan, A.A.P. Khan, P. Singh, E. Lichtfouse, C. Wang, T. Huong, Advanced activation of persulfate by polymeric g-C_3N_4 based photocatalysts for environmental remediation: a review. J. Hazard. Mater. **413**, 125324 (2021)
8. V. Dutta, P. Singh, P. Shandilya, S. Sharma, P. Raizada, A.K. Saini, V.K. Gupta, A. Hosseini-Bandegharaei, S. Agarwal, A. Rahmani-Sani, Review on advances in photocatalytic water disinfection utilizing graphene and graphene derivatives-based nanocomposites. J. Environ. Chem. Eng. **7**, 103132 (2019)
9. Y. Gao, Z. Zhang, S. Li, J. Liu, L. Yao, Y. Li, H. Zhang, Insights into the mechanism of heterogeneous activation of persulfate with a clay/iron-based catalyst under visible LED light irradiation. Appl. Catal. B **185**, 22–30 (2016)
10. F. Chen, G.X. Huang, F.B. Yao, Q. Yang, Y.M. Zheng, Q.B. Zhao, H.Q. Yu, Catalytic degradation of ciprofloxacin by a visible-light-assisted peroxymonosulfate activation system: performance and mechanism. Water Res. **173**, 115559 (2020)
11. G.N. Coulibaly, S. Bae, J. Kim, A.A. Assadi, K. Hanna, Enhanced removal of antibiotics in hospital wastewater by Fe–ZnO activated persulfate oxidation. Environ. Sci. **5**, 2193–2201 (2019)
12. Q. Feng, J. Zhou, Y. Zhang, Coupling Bi_2MoO_6 with persulfate for photocatalytic oxidation of tetracycline hydrochloride under visible light. J. Mater. Sci.: Mater. Electron. **30**, 19108–19118 (2019)
13. J. Bedia, V. Muelas-Ramos, M. Peñas-Garzón, A. Gómez-Avilés, J. Rodríguez, C. Belver, A review on the synthesis and characterization of metal organic frameworks for photocatalytic water purification. Catalysts **9**, 52 (2019)
14. C.-C. Wang, Y.-Q. Zhang, J. Li, P. Wang, Photocatalytic CO_2 reduction in metal–organic frameworks: a mini review. J. Mol. Struct. **1083**, 127–136 (2015)
15. E.M. Dias, C. Petit, Towards the use of metal–organic frameworks for water reuse: a review of the recent advances in the field of organic pollutants removal and degradation and the next steps in the field. J. Mater. Chem. A **3**, 22484–22506 (2015)
16. Y. Wen, M. Feng, P. Zhang, H.-C. Zhou, V.K. Sharma, X. Ma, Metal organic frameworks (MOFs) as photocatalysts for the degradation of agricultural pollutants in water. ACS ES&T Eng. **1**, 804–826 (2021)
17. C.-W. Huang, V.-H. Nguyen, S.-R. Zhou, S.-Y. Hsu, J.-X. Tan, K.C.W. Wu, Metal–organic frameworks: preparation and applications in highly efficient heterogeneous photocatalysis. Sust. Energy Fuels **4**, 504–521 (2020)
18. K.A. Kovalenko, N.V. Ruban, S.A. Adonin, D.V. Korneev, S.B. Erenburg, S.V. Trubina, K. Kvashnina, M.N. Sokolov, V.P. Fedin, Bi(iii) immobilization inside MIL-101: enhanced photocatalytic performance. New J. Chem. **41**, 2255–2260 (2017)
19. L. Shi, L. Yang, H. Zhang, K. Chang, G. Zhao, T. Kako, J. Ye, Implantation of Iron(III) in porphyrinic metal organic frameworks for highly improved photocatalytic performance. Appl. Catal. B **224**, 60–68 (2018)
20. X. Pan, L. Yan, R. Qu, Z. Wang, Degradation of the UV-filter benzophenone-3 in aqueous solution using persulfate activated by heat, metal ions and light. Chemosphere. **196**, 95–104 (2018)
21. Z. Wang, J. Huang, J. Mao, Q. Guo, Z. Chen, Y. Lai, Metal–organic frameworks and their derivatives with graphene composites: preparation and applications in electrocatalysis and photocatalysis. J. Mater. Chem. A **8**, 2934–2961 (2020)
22. Y. Gong, B. Yang, H. Zhang, X. Zhao, A g-C_3N_4/MIL-101(fe) heterostructure composite for highly efficient BPA degradation with persulfate under visible light irradiation. J. Mater. Chem. A **6**, 23703–23711 (2018)
23. S. Miao, Z. Zha, Y. Li, X. Geng, J. Yang, S. Cui, J. Yang, Visible-light-driven MIL-53(Fe)/BiOCl composite assisted by persulfate: photocatalytic performance and mechanism. J. Photochem. Photobiol., A **380**, 111862 (2019)
24. Q. Feng, J. Gu, Q. Rong, M. Liang, X. Zhou, S. Li, Z. Xu, Li, Porous dual Z-scheme InOOH/RCN/$CoWO_4$ heterojunction with enhanced photothermal-photocatalytic properties towards norfloxacin degradation. Sep. Purif. Technol. **308**, 122890 (2023)
25. C. Feng, Z. Lu, Y. Zhang, Q. Liang, M. Zhou, X. Li, C. Yao, Z. Li, S. Xu, A magnetically recyclable dual Z-scheme GCNQDs-$CoTiO_3$/$CoFe_2O_4$ composite photocatalyst for efficient photocatalytic degradation of oxytetracycline. Chem. Eng. J. **435**, 134833 (2022)
26. H. Wang, X. Yuan, Y. Wu, G. Zeng, X. Chen, L. Leng, H. Li, Synthesis and applications of novel graphitic carbon nitride/metal-organic frameworks mesoporous photocatalyst for dyes removal. Appl. Catal. B **174–175**, 445–454 (2015)
27. H. Wang, L. Zhang, Z. Chen, J. Hu, S. Li, Z. Wang, J. Liu, X. Wang, Semiconductor heterojunction photocatalysts:

design, construction, and photocatalytic performances. Chem. Soc. Rev. **43**, 5234–5244 (2014)
28. Y.-C. Zhou, X.-Y. Xu, P. Wang, H. Fu, C. Zhao, C.-C. Wang, Facile fabrication and enhanced photocatalytic performance of visible light responsive UiO-66-NH_2/Ag_2CO_3 composite. Chin. J. Catal. **40**, 1912–1923 (2019)
29. A.A. Alqadami, M.A. Khan, M.R. Siddiqui, Z.A. Alothman, Development of citric anhydride anchored mesoporous MOF through post synthesis modification to sequester potentially toxic lead (II) from water. Microporous Mesoporous Mater. **261**, 198–206 (2018)
30. L. Wang, X. Ma, G. Huang, R. Lian, J. Huang, H. She, Q. Wang, Construction of ternary CuO/$CuFe_2O_4$/g-C_3N_4 composite and its enhanced photocatalytic degradation of tetracycline hydrochloride with persulfate under simulated sunlight. J. Environ. Sci. (China). **112**, 59–70 (2022)
31. Y. Pan, D. Li, H.L. Jiang, Sodium-doped C_3N_4/MOF heterojunction composites with tunable band structures for photocatalysis: interplay between light harvesting and electron transfer. Chemistry **24**, 18403–18407 (2018)
32. M. Kandiah, M.H. Nilsen, S. Usseglio, S. Jakobsen, U. Olsbye, M. Tilset, C. Larabi, E.A. Quadrelli, F. Bonino, Lillerud, synthesis and stability of tagged UiO-66 Zr-MOFs. Chem. Mater. **22**, 6632–6640 (2010)
33. M.A. Gotthardt, A. Beilmann, R. Schoch, J. Engelke, W. Kleist, Post-synthetic immobilization of palladium complexes on metal–organic frameworks–a new concept for the design of heterogeneous catalysts for heck reactions. RSC Adv. **3**, 10676–10679 (2013)
34. G. Fan, J. Zhan, J. Luo, J. Lin, F. Qu, B. Du, Y. You, Z. Yan, Fabrication of heterostructured Ag/AgCl@g-C_3N_4@UIO-66(NH_2) nanocomposite for efficient photocatalytic inactivation of *Microcystis aeruginosa* under visible light. J. Hazard. Mater. **404**, 124062 (2021)
35. J. Xu, J. Gao, Y. Qi, C. Wang, L. Wang, Anchoring Ni_2P on the UiO-66-NH_2/g-C_3N_4-derived C-doped ZrO_2/g-C_3N_4 heterostructure: highly efficient photocatalysts for H_2 production from water splitting. ChemCatChem **10**, 3327–3335 (2018)
36. R. Li, M. Cai, Z. Xie, Q. Zhang, Y. Zeng, H. Liu, G. Liu, W. Lv, Construction of heterostructured $CuFe_2O_4$/g-C_3N_4 nanocomposite as an efficient visible light photocatalyst with peroxydisulfate for the organic oxidation. Appl. Catal. B **244**, 974–982 (2019)
37. S.-W. Lv, X. Wang, X. Wei, Y. Zhang, Y. Cong, L. Che, Introduction of cluster-to-metal charge transfer in UiO-66-NH_2 for enhancing photocatalytic degradation of bisphenol a in the existence of peroxymonosulfate. Sep. Purif. Technol. **292**, 121018 (2022)
38. Q. Liang, M. Zhang, Z. Zhang, C. Liu, S. Xu, Z. Li, Zinc phthalocyanine coupled with UIO-66 (NH_2) via a facile condensation process for enhanced visible-light-driven photocatalysis. J. Alloys Compd. **690**, 123–130 (2017)
39. Y. Su, Z. Zhang, H. Liu, Y. Wang, $Cd_{0.2}Zn_{0.8}S$@UiO-66-NH_2 nanocomposites as efficient and stable visible-light-driven photocatalyst for H_2 evolution and CO_2 reduction. Appl. Catal. B **200**, 448–457 (2017)
40. Y. Sun, Y. Gu, P. Zhang, Adsorption properties and recognition mechanisms of a novel surface imprinted polymer for selective removal of Cu(II)-citrate complexes. J. Hazard. Mater. **424**, 127735 (2022)
41. Y. Zhang, M. Zhou, A critical review of the application of chelating agents to enable Fenton and Fenton-like reactions at high pH values. J. Hazard. Mater. **362**, 436–450 (2019)
42. L. Xie, T. Zhang, X. Wang, W. Zhu, Z. Liu, M. Liu, J. Wang, L. Zhang, T. Du, C. Yang, M. Zhu, J. Wang, Facile construction of Fe^{3+}/Fe^{2+} mediated charge transfer pathway in MIL-101 for effective tetracycline degradation. J. Clean. Prod. **359**, 131808 (2022)
43. H. Sun, F. Guo, J. Pan, W. Huang, K. Wang, W. Shi, One-pot thermal polymerization route to prepare N-deficient modified g-C_3N_4 for the degradation of tetracycline by the synergistic effect of photocatalysis and persulfate-based advanced oxidation process. Chem. Eng. J. **406**, 126844 (2021)
44. Z. Liu, Z. Gao, Q. Wu, Activation of persulfate by magnetic zirconium-doped manganese ferrite for efficient degradation of tetracycline. Chem. Eng. J. **423**, 130283 (2021)
45. Q. He, M. Ge, Visible-light activation of peroxydisulfate by magnetic BiOBr/$MnFe_2O_4$ nanocomposite toward degradation of tetracycline. J. Mater. Sci.: Mater. Electron. **33**, 5859–5877 (2022)
46. B. Liu, W. Song, W. Zhang, X. Zhang, S. Pan, H. Wu, Y. Sun, Y. Xu, Fe_3O_4@CNT as a high-effective and steady chainmail catalyst for tetracycline degradation with peroxydisulfate activation: performance and mechanism. Sep. Purif. Technol. **273**, 118705 (2021)
47. G. Chen, Y. Yu, L. Liang, X. Duan, R. Li, X. Lu, B. Yan, N. Li, S. Wang, Remediation of antibiotic wastewater by coupled photocatalytic and persulfate oxidation system: a critical review. J. Hazard. Mater. **408**, 124461 (2021)
48. C. Zhao, Y. Li, H. Chu, X. Pan, L. Ling, P. Wang, H. Fu, C.C. Wang, Z. Wang, Construction of direct Z-scheme Bi_5O_7I/UiO-66-NH_2 heterojunction photocatalysts for enhanced degradation of ciprofloxacin: mechanism insight, pathway analysis and toxicity evaluation. J. Hazard. Mater. **419**, 126466 (2021)
49. F. Liu, H. Zhou, Z. Pan, Y. Liu, G. Yao, Y. Guo, B. Lai, Degradation of sulfamethoxazole by cobalt-nickel powder

composite catalyst coupled with peroxymonosulfate: performance, degradation pathways and mechanistic consideration. J. Hazard. Mater. **400**, 123322 (2020)
50. X.-W. Zhang, F. Wang, C.-C. Wang, P. Wang, H. Fu, C. Zhao, Photocatalysis activation of peroxodisulfate over the supported Fe_3O_4 catalyst derived from MIL-88A(Fe) for efficient tetracycline hydrochloride degradation. Chem. Eng. J. **426**, 131927 (2021)
51. C. Zhao, J. Wang, X. Chen, Z. Wang, H. Ji, L. Chen, W. Liu, C.C. Wang, Bifunctional $Bi_{12}O_{17}Cl_2$/MIL-100(fe) composites toward photocatalytic cr(VI) sequestration and activation of persulfate for bisphenol A degradation. Sci. Total Environ. **752**, 141901 (2021)
52. E. Saputra, S. Muhammad, H. Sun, H.M. Ang, M.O. Tade, S. Wang, Different crystallographic one-dimensional MnO_2 nanomaterials and their superior performance in catalytic phenol degradation. Environ. Sci. Technol. **47**, 5882–5887 (2013)
53. H. Liu, J. Zhang, D. Ao, Construction of heterostructured $ZnIn_2S_4$@NH_2-MIL-125(Ti) nanocomposites for visible-light-driven H_2 production. Appl. Catal. B **221**, 433–442 (2018)
54. Z. Sha, J. Wu, Enhanced visible-light photocatalytic performance of BiOBr/UiO-66(zr) composite for dye degradation with the assistance of UiO-66. RSC Adv. **5**, 39592–39600 (2015)
55. L.-P. Zhang, J.-R. Ran, S.-Z. Qiao, M. Jaroniec, Characterization of semiconductor photocatalysts. Chem. Soc. Rev. **48**, 5184–5206 (2019)
56. A. Hankin, F.E. Bedoya-Lora, J.C. Alexander, A. Regoutz, G.H. Kelsall, Flat band potential determination: avoiding the pitfalls. J. Mater. Chem. A **7**, 26162 (2019)
57. D. Roy, S. Neogi, S. De, Visible light assisted activation of peroxymonosulfate by bimetallic MOF based heterojunction MIL-53(Fe/Co)/CeO_2 for atrazine degradation: pivotal roles of dual redox cycle for reactive species generation. Chem. Eng. J. **430**, 133069 (2022)
58. X.-H. Yi, S.-Q. Ma, X.-D. Du, C. Zhao, H. Fu, P. Wang, C.-C. Wang, The facile fabrication of 2D/3D Z-scheme g-C_3N_4/UiO-66 heterojunction with enhanced photocatalytic Cr(VI) reduction performance under white light. Chem. Eng. J. **375**, 121944 (2019)
59. C.-C. Wang, X.-D. Du, J. Li, X.-X. Guo, P. Wang, J. Zhang, Photocatalytic cr(VI) reduction in metal-organic frameworks: a mini-review. Appl. Catal. B **193**, 198–216 (2016)
60. N. Li, S. Tang, Y. Rao, J. Qi, Q. Zhang, D. Yuan, Peroxymonosulfate enhanced antibiotic removal and synchronous electricity generation in a photocatalytic fuel cell. Electrochim. Acta. **298**, 59–69 (2019)
61. H. Xie, M. Luo, W. Huang, Y. Huang, X. Feng, Z. Xu, W. Luo, S. Wang, H. Lin, G. Mailhot, Application and mechanism of ferrihydrite in the EDDS improved heterogeneous photo-Fenton system: the role of different reactive species under different conditions. New J. Chem. **44**, 7602–7610 (2020)
62. A. Ghauch, A.M. Tuqan, N. Kibbi, Naproxen abatement by thermally activated persulfate in aqueous systems. Chem. Eng. J. **279**, 861–873 (2015)
63. S. Tang, X. Li, C. Zhang, Y. Liu, W. Zhang, D. Yuan, Strengthening decomposition of oxytetracycline in DBD plasma coupling with Fe–Mn oxide-loaded granular activated carbon. Plasma Sci. Technol. **21**, 025504 (2019)
64. Y. Yang, C. Zhang, D. Huang, G. Zeng, J. Huang, C. Lai, C. Zhou, W. Wang, H. Guo, W. Xue, R. Deng, M. Cheng, W. Xiong, Boron nitride quantum dots decorated ultrathin porous g-C_3N_4: intensified exciton dissociation and charge transfer for promoting visible-light-driven molecular oxygen activation. Appl. Catal. B **245**, 87–99 (2019)
65. A. Wang, Z. Chen, Z. Zheng, H. Xu, H. Wang, K. Hu, K. Yan, Remarkably enhanced sulfate radical-based photo-Fenton-like degradation of levofloxacin using the reduced mesoporous MnO@MnO_x microspheres. Chem. Eng. J. **379**, 122340 (2020)
66. B. Xu, Z. Chen, B. Han, C. Li, Glycol assisted synthesis of MIL-100(fe) nanospheres for photocatalytic oxidation of benzene to phenol. Catal Commun. **98**, 112–115 (2017)
67. B. Kordestani, R. Jalilzadeh Yengejeh, A. Takdastan, A.K. Neisi, A new study on photocatalytic degradation of meropenem and ceftriaxone antibiotics based on sulfate radicals: influential factors, biodegradability, mineralization approach. Microchem. J. **146**, 286–292 (2019)